

Optical Design of Multilayer Achromatic Waveplate by Simulated Annealing Algorithm

Jun Ma¹, Jing-Shan Wang^{2,4}, Carsten Denker³ and Hai-Min Wang^{1,2}

¹ Big Bear Solar Observatory 40386 North Shore Lane, Big Bear City, CA 92314, USA
jxm1901@njit.edu

² New Jersey Institute of Technology, Center for Solar-Terrestrial Research, 323 Martin Luther King Blvd., Newark, NJ 07102, USA

³ Astrophysikalisches Institut Potsdam, An der Sternwarte 16, D-14482 Potsdam, Germany

⁴ Currently working at Thorlabs, Inc., 435 Route 206, Newton, NJ 07860, USA

Received 2007 May 22; accepted 2007 December 14

Abstract We applied a Monte Carlo method — simulated annealing algorithm — to carry out the design of multilayer achromatic waveplate. We present solutions for three-, six- and ten-layer achromatic waveplates. The optimized retardance settings are found to be $89^{\circ}51'39'' \pm 0^{\circ}33'37''$ and $89^{\circ}54'46'' \pm 0^{\circ}22'4''$ for the six- and ten-layer waveplates, respectively, for a wavelength range from 1000 nm to 1800 nm. The polarimetric properties of multilayer waveplates are investigated based on several numerical experiments. In contrast to previously proposed three-layer achromatic waveplate, the fast axes of the new six- and ten-layer achromatic waveplate remain at fixed angles, independent of the wavelength. Two applications of multilayer achromatic waveplate are discussed, the general-purpose phase shifter and the birefringent filter in the Infrared Imaging Magnetograph (IRIM) system of the Big Bear Solar Observatory (BBSO). We also checked an experimental method to measure the retardance of waveplates.

Key words: instrumentation: spectrographs — methods: numerical — methods: laboratory — Sun: infrared

1 INTRODUCTION

Waveplate is a birefringent optical component that can produce a predefined phase retardance between two orthogonal components (polarized components) of the amplitude vector of the light. Unfortunately, for naturally available material, such as quartz or calcite, the retardance of a waveplate is a function of both the wavelength of incoming light and its working temperature. The temperature can be controlled in practice; however, this is not the case for the wavelength. Many instruments are designed to operate at different wavelengths, such as the near infrared tunable birefringent filter (NIRTF) designed for the Advanced Technology Solar Telescope (ATST) (Keil et al. 2001, 2005; Rimmele et al. 2005), and the Near Infrared Imaging Magnetograph (IRIM) (Denker et al. 2003a,b) for the New Solar Telescope (NST) (Denker et al. 2006; Goode & NST Team 2006). As central optical components in many of these instruments, waveplates which can only produce certain phase retardance at single wavelengths have become one of the major issues to be solved.

2 METHODS OF DESIGN

There are basically two approaches to the optical design of an achromatic waveplate: crystalline and form-birefringence waveplates. A crystalline waveplate (Fig. 1) is an optical train of slabs of birefringent mate-

rials. Both the thicknesses d_k and the azimuth θ_k are to be so specified as to reduce the wavelength dependence of the retardance. This is the one used in our current study and we will refer to it as the “ n -layer” or multilayer waveplate. A form-birefringence waveplate is a single layer of material, not necessarily birefringent, but with embedded periodic surface structures on micron- or nano-scales. Such small structures produce the form birefringence (Born & Wolf 1999), which can be used to build achromatic waveplates (Kikuta et al. 1997; Flanders 1983). This approach relies on semiconductor manufacturing technology that is beyond the scope of this presentation.

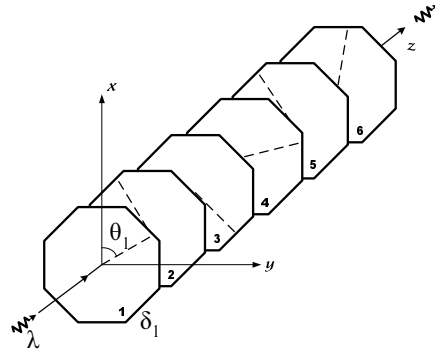


Fig. 1 Diagram of a six-layer waveplate. Dashed lines indicate the optical axes of the crystals, and are for demonstration purpose only.

The idea of using three layers of birefringent material to achieve achromatic waveplate was initiated by Pancharatnam (1955). The method was further developed by various authors. For example, an analytical design of three-layer achromatic waveplates can be found in Title (1975) with specified retardances of 115.5° , 180° and 115.5° and azimuths of 0° , 70.6° and 0° for a three-layer $\lambda/4$ waveplate. For a three-layer half waveplate, the retardances are 180° , 180° , 180° and the azimuths are 0° , 60° , 0° . A different computational approach of designing six- and ten-layer achromatic waveplates was presented by McIntyre & Harris (1968), who presented both numerical and experimental results. In this unique design, the waveplates all have the same thicknesses but different azimuths. The achromatic range considered was 400 to 800 nm. Various other designs exist using two different birefringent materials (e.g., Beckers 1971; Beckers 1972; Hariharan 1995; Guimond & Elmore 2004) or prisms (Filinski & Skettrup 1984). One issue in these designs is that the optical-axes of the assembled waveplates also vary with the wavelength. The multilayer (more than three layers) waveplates investigated in this paper is a solution to this issue.

2.1 Defining the Optimization Problem

Our definition of an achromatic waveplate is that a multilayer structure which has an almost constant Jones matrix within a certain wavelength range. The definition implies equivalence between a Jones matrix and a waveplate.

In Figure 1, $\mathbf{J}_{\text{awp}} = \mathbf{J}_1 \cdot \mathbf{J}_2 \cdot \mathbf{J}_3 \cdot \dots \cdot \mathbf{J}_n$ stands for the total Jones matrix of the multilayer waveplate and $\mathbf{J}_{\text{perfect}}$ is the Jones matrix of an ideal waveplate with a predefined retardance. Each \mathbf{J}_k depends on a set of parameters θ_k and δ_k with $k = 1, \dots, n$, which are the azimuth and retardance of each layer, respectively. The design criterion of an n -layer achromatic waveplate is to minimize the following merit function,

$$E(\theta_k, \delta_k) = \sum_{\lambda, i, j} \Delta J_{ij} \cdot \Delta J_{ij}^*, \quad (1)$$

$$\text{with } \delta_k = 2\pi\mu(\lambda)d_k/\lambda. \quad (2)$$

The matrix $\Delta\mathbf{J} = \mathbf{J}_{\text{awp}} - \mathbf{J}_{\text{perfect}}$ represents the Jones matrix difference between an n -layer waveplate and the ideal waveplate, which has four elements. One way to arrange the summation in Equation (1) is

to sample a large number (> 100) of equally spaced points between 1000 to 1800 nm. This arrangement implies that every sampled wavelength is equally important. If there are any spectral lines of particular interest, then the merit function can be evaluated only at these locations such that the final design will be particularly optimized in the vicinity of these spectral lines. The wavelength dispersion of the birefringence μ can be found in Ghosh (1999), in which are listed the experimental data of the refractive indices for both quartz and calcite at different wavelengths. For quartz, in the wavelength range from 1000 nm to 1800 nm, a simple regression relation can be found:

$$\mu(\lambda) = a + b\lambda + c\lambda^2, \quad (3)$$

where $a = 0.009134$, $b = -2.65 \times 10^{-7}$ and $c = -1.04 \times 10^{-10}$.

The merit function defined in Equation (1) has $n \times 2$ free parameters and is highly non-linear. A cursory investigation of this function shows that it possesses a large number of local minima. Many of the standard minimization methods for global optimization problems will fail to locate and rank these local minima. In this study, we attack the nonlinear optimization problem of minimizing Equation (1) using the simulated annealing (SA) algorithm invented by Kirkpatrick et al. (1983).

2.2 The Simulated Annealing Algorithm

The SA algorithm is a generalized Monte Carlo algorithm invented by Kirkpatrick et al. (1983) and has been successfully applied to many scientific and engineering problems (e.g., Habib et al. 2006; Sun et al. 2005). For the details of the development of the SA algorithm, we refer to the original work by Kirkpatrick et al. (1983), the monograph on Monte Carlo method by Newman & Barkema (1999) and a series of papers by Ingber (1996). The basic principle of SA computing algorithm resembles a real physical phenomena — in the annealing of melted materials, the system in equilibrium described by Gibbs statistics approaches the ground state if the annealing temperature decreases to zero slowly enough.

At the starting point of an SA program, the system represented by the energy E (parameterized by a set of free parameters) is put at a high temperature (“hypothetical temperature”), e.g., $T_0 = 5$. Note that this temperature is only a concept borrowed from statistical mechanics, and has nothing to do with real temperature. It is a controlling factor of the randomness in state space. This temperature is slowly reduced based on a predefined annealing schedule. At each temperature, the system is allowed to stay long enough to achieve an equilibrium state while the state space (a non-convex hyperspace of free parameters) is sampled according to a predefined sampling probability. Each state in the state space corresponds to an energy state. The transition from one energy state E_1 to another E_2 is controlled by the Metropolis algorithm — if $E_2 < E_1$, the shift in the state space will be accepted. Otherwise, it will be accepted with the probability given by

$$P_{12} = \exp\left(-\frac{E_2 - E_1}{T}\right). \quad (4)$$

It can be shown that any Monte Carlo simulation utilizing the Metropolis algorithm will statistically converge to a steady state (as long as it exists), since the algorithm satisfies the condition of detailed balance.

We modify the “energy of system” defined in Equation (1) by including a 2×2 constant weighting matrix w in the definition,

$$E = \sum_{\lambda} \sum_{ij} w_{ij} \Delta J_{ij} \cdot \Delta J_{ij}^*, \quad (5)$$

where the weighting factors are set to be $w_{12} = w_{21} = 100$ and $w_{11} = w_{22} = 1$. The two off diagonal elements of the Jones matrix of an ideal waveplate are precisely zero. For a multilayer achromatic waveplate, any non-zero residuals in these two matrix elements will introduce significant (optical) errors in the final achromatic waveplate. The weighting factors will guide the SA simulation to identify “energy states” corresponding to Jones matrices having the off-diagonal elements smaller. The design results in Figure 2 are based on this strategy.

As shown by Kirkpatrick et al. (1983) and Munakata & Nakamura (2001), the annealing schedule is critical to the performance of the algorithm. We took a simple approach to schedule the annealing process.

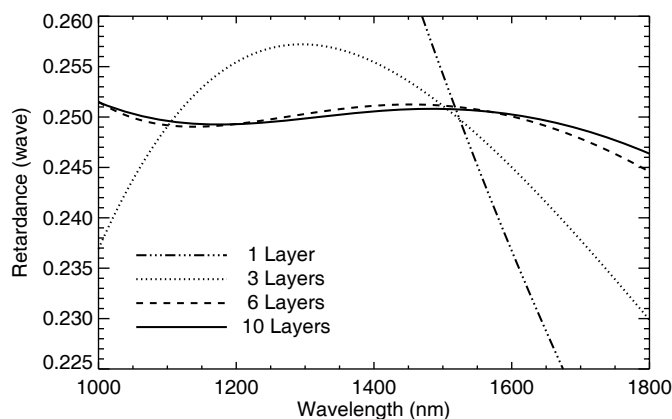


Fig. 2 Retardance vs. wavelength (computational).

Table 1 Configurations of the n -Layer Achromatic Waveplates.

Waveplate Type	Layer Indices	$\theta_i(n=3)$	$\delta_i(n=3)$	$\theta_i(n=6)$	$\delta_i(n=6)$	$\theta_i(n=10)$	$\delta_i(n=10)$
$\lambda/4$ waveplates	1	2.60597	1.67497	1.07182	2.04183	0.42316	3.14500
	2	0.68614	2.60756	2.93447	2.62344	1.97316	2.31108
	3	2.60616	1.67451	1.76245	0.09279	2.61497	2.96516
	4			2.03863	3.46254	1.04133	4.27803
	5			0.45159	1.04843	1.16881	1.31223
	6			0.28911	3.49240	2.81640	3.19563
	7					2.28689	3.75644
	8					0.64636	2.34117
	9					0.24218	0.47576
	10					0.39315	1.28262
$\lambda/2$ waveplates	1	0.51334	2.60841	0.38862	2.41938	0.45642	1.94016
	2	2.62775	2.60876	1.02418	2.40367	2.39951	2.71146
	3	0.51278	2.60825	2.75162	6.27907	0.65613	4.17675
	4			0.68827	0.87668	2.55021	5.39916
	5			1.54634	1.14318	2.60234	0.03210
	6			0.54589	3.00237	0.85728	2.48566
	7					0.34136	3.53937
	8					2.67365	0.75042
	9					1.44123	0.60797
	10					1.78125	1.37686

Whenever we find the system energy stalled at one temperature after 20000 function calls to the merit function, we reduce the temperature by multiplying a factor, i.e.,

$$T_{t+1} = cT_t, \quad (6)$$

where the subscription t records the occasions of decreasing the temperature. In our computing program, we chose $c = 0.95$. Although this is not a rigorous treatment, it produces reasonably accurate results, see Table 1.

2.3 Comments on the Computed Results

The analysis in Title (1975) showed that, using same uniaxial material, at least three layers are required in order to form a multilayer waveplate. We reconfirmed this conclusion by observing that a two-layer waveplate system will not reach a sufficiently low energy state, even if the effective temperature has been reduced to zero. For a multilayer waveplate with more than two layers, the energy reduces uniformly as the

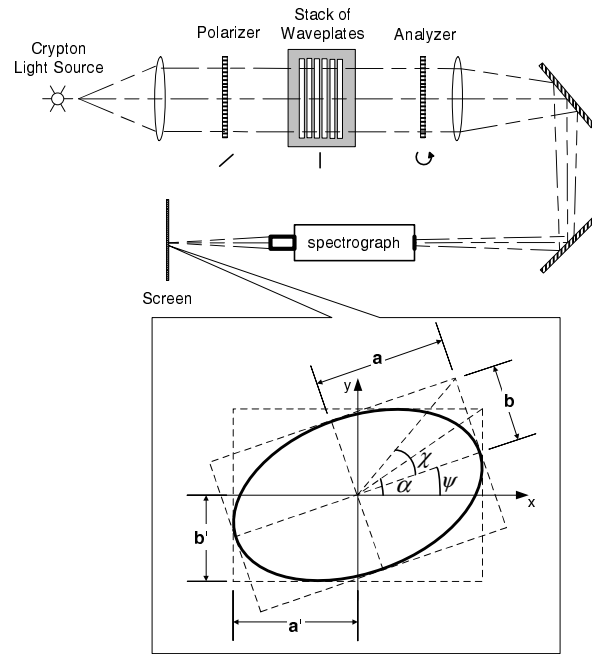


Fig. 3 Measurement of retardance. Shown in the waveplate-stack is the six-layer achromatic $\lambda/4$ -waveplate.

temperature decreases. The results of the SA algorithm are collected in Table 1, which includes three-, six- and ten-layer achromatic waveplate designs.

Note that in the three-layer $\lambda/4$ waveplate configuration in Table 1, the first and third layers have very similar parameters. Similarly, all layers of the three-layer $\lambda/2$ waveplate have roughly the same retardance. These results agree with the results based on the analytical method in Title (1975). However, there exist quantitative differences between the computed configurations and analytical counterparts. This is due to the different definitions of the optimization. As defined by Equation (1) or Equation (5), the error of the computed configurations are “globally” optimized from 1000 to 1800 nm. The analytical configurations were optimized locally.

3 NUMERICAL EVALUATION OF THE OPTICAL PERFORMANCE OF THE N -LAYER ACHROMATIC WAVEPLATES

Optical components used in polarimetry can be represented by 2×2 Jones matrices and 4×4 Mueller matrices. A full introduction of the development and applications of these two formalisms used in polarization optics can be found in a monograph (Shurcliff 1966).

3.1 Normal Incidence

First, let us assume that the incoming monochromatic light incidents perpendicularly. In this experiment, the waveplates are set up between two linear polarizers (see the experimental arrangement in Fig. 3). The active angle of the first polarizer is set to 45° with respect to the optical axes of the waveplates. The second polarizer is rotated on its azimuth axis. If the waveplates are assumed to be perfect $\lambda/4$ waveplates, the output intensity shall be constant as the second polarizer is rotated. However, the computational results show that the ratio between the maximum intensity and the minimum intensities, i.e., the ellipticity of the ellipse, is not necessarily unity — the output light after passing through the multilayer $\lambda/4$ waveplate is elliptically polarized.

On the other hand, the larger deviation from unity of the ellipticity of the testing light beam shown for the three-layer waveplate is expected from previous studies (Ma et al. 2004; Beckers 1971;

Beckers et al. 1975), since the effective optical axis of a three-layer achromatic waveplate rotates to different angles at different wavelengths. The performance of the three-layer achromatic waveplate at the two wavelengths He I 1083 nm and Fe I 1565 nm is better than any globally optimized solutions for the six- and ten-layer cases. The application of such three-layer waveplate in IRIM of BBSO will be investigated in Section 4.2, since IRIM is specifically designed for polarimetry observations at the two wavelengths.

Given the ellipticity of the testing light obtained in the above mentioned method, the retardance can be derived by using the method shown in Appendix 5. The corresponding results are displayed in Figure 2, which plots the retardance of the single-, three-, six-, and ten-layer quarter waveplates. Over the wavelength range from 1000 nm to 1800 nm, the maximum error of the ten-layer achromatic $\lambda/4$ waveplate is approximately 0.3% wave, or equivalently, 1° . As will be discussed in later sections, the retardance error of this magnitude is negligible in the application of a birefringent filter or a phase shifter.

The second experiment is concerned with the polarization transformation properties of n -layer achromatic waveplates. Let the incoming light be linearly polarized. Then it can be shown that the Stokes vector of linear polarized light along direction α with respect to the x -axis is

$$\mathbf{S} = [1, \cos^2 \alpha - \sin^2 \alpha, 2 \sin \alpha \cos \alpha, 0]^T. \quad (7)$$

Let \mathbf{S}_{in} be the Stokes vector of the incoming light. Then, the output is $\mathbf{S}_{\text{out}} = \mathbf{M}_{\text{awp}} \cdot \mathbf{S}_{\text{in}}$, where \mathbf{M}_{awp} is the Mueller matrix of the n -layer achromatic waveplate (see Fig. 4). All waveplates are rotated by an arbitrary angle of 108° with respect to the x -axis, which simulates a snapshot of a rotating waveplate. The simulation shows that, after passing through a $\lambda/4$ waveplate, the polarization energy is re-distributed among Q, U, V -components and causes varying polarization errors, for instance, in the measurement of the vector magnetic field of the Sun (Kuhn et al. 1994). In measuring solar magnetic fields, the Q - and U -components are directly related to the transversal magnetic field. The V -component is related to the longitudinal field. Therefore, crosstalk of the V -component due to the polarization error of the waveplate can appear as spurious magnetic signal in the Q -component. This was observed before — in the calibration of DVMG system at BBSO, the Stokes- V signals can be identified in the Stokes- Q image, when the optical axis and retardance of the ferroelectric crystal (FLC) is not accurate (Spirock 2005).

In Figure 4, the crosstalk of the n -layer waveplate is roughly limited to 2% across the specified wavelength range. Note that only the linearly polarized light has been considered in this numerical experiment. In order to fully understand the polarimetric characteristics of the n -layer waveplate, the elements of the Muller matrices need to be investigated for distinct wavelengths and for different azimuths. We will only consider the elements $M(i, j)$ with $i, j = 2, 3, 4$, which define the crosstalk among the linear and circular polarizations. Let

$$\Delta \mathbf{M} = \mathbf{M}_{10} - \mathbf{M}_{\text{ideal}} \quad (8)$$

be the difference between the Muller matrices of a ten-layer quarter waveplate (\mathbf{M}_{10}) and an ideal quarter waveplate ($\mathbf{M}_{\text{ideal}}$).

3.2 Orientation of the Optical Axes of n -Layer Waveplates

The optical axes of Pancharatnam-type achromatic waveplates (Pancharatnam 1955) rotate to distinct angles at different wavelengths (Beckers et al. 1975). This issue would be minimized in the six- and ten-layer achromatic waveplates. In the criterion of optimization defined by Equation (5), $\Delta \mathbf{J}$ is the difference between the n -layer waveplate and an ideal waveplate. Therefore, the minimization of ΔE corresponds to finding an n -layer waveplate, whose Jones matrix is closest to that of an ideal waveplate. The optical axes of the n -layer waveplate shall overlap with the optical axes of an ideal waveplate across the whole wavelength range defined in the optimization, which is zero.

In Figure 4, it is also shown indirectly that the azimuth of optical axes of the six- and ten-layer achromatic waveplates can not change greatly within the specified wavelength range. Direct evaluation of the azimuth of optical axis involves the decomposition of complex Jones matrices and other complicated algebra operations, which we did not venture to do in the present paper.

4 CASE STUDIES

In this section, we apply the achromatic waveplates listed in Table 1 to various applications. Some of these examples are general enough to be used in fields besides solar physics.

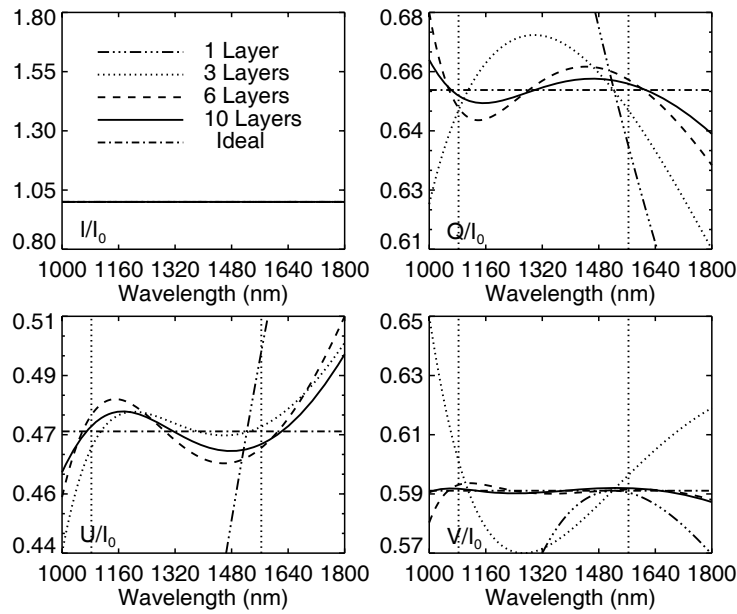


Fig. 4 Simulated polarization crosstalk of n -layer $\lambda/4$ waveplates (see Table 1 for parameters of each layer). The two vertical straight lines indicate the locations of wavelengths 1083 nm and 1565 nm. The effective optical axis of the overall stack of the achromatic waveplates is rotated by 108° (an arbitrarily chosen angle) to the x -axis. The incident light is linearly polarized and the angle between its polarization axis and the x -axis is $\pi/5$. The corresponding Stokes vector of the light is $[1, \cos^2 \frac{\pi}{5} - \sin^2 \frac{\pi}{5}, 2 \cos \frac{\pi}{5} \sin \frac{\pi}{5}, 0]$.

4.1 Phase Shifting Unit

Phase shifting unit is an instrument that produces a continuous fractional phase difference between two perpendicularly polarized light. Several theoretical approaches are discussed in Evans (1949) to realize phase shifters. One of these consists of a combination of one $\lambda/2$ waveplate sandwiched in between two $\lambda/4$ waveplates, which is particularly interesting due to its flexibility. We will check this approach by substituting the normal birefringent crystals with six-layer achromatic waveplates arranged in a fashion of $(\lambda/4 \leftrightarrow \lambda/2 \leftrightarrow \lambda/4)$ with properly aligned optical axes.

The optical axes of both the first waveplate unit ($\lambda/4$) and the third waveplate unit ($\lambda/4$) are set to 45° with respect to the polarization direction of the incident light, which, without loss of generality, we chose to be the x -axis. The second waveplate ($\lambda/2$) sits on a rotary stage driven by a motor and its azimuthal angle θ is measured with respect to the x -axis. In Figure 5, the elements of the Jones matrices of the phase shifters are examined. The retardance of a phase shifter is derived from the two diagonal elements of the Jones matrix, see Figure 5a. In Figure 5b, the amplitude of one off-diagonal element (complex number) is plotted. The solid curve represents the phase shifter made of six-layer achromatic waveplates, which are almost zero. As a comparison, we also plot the Jones matrix off-diagonal element of a phase shifter made of three single-crystal waveplates (dashed curves). The corresponding Jones matrix has comparatively large off-diagonal elements. Large off-diagonal elements of the Jones matrix usually imply that the optical axis of the retarder is rotated by an undetermined angle.

Figure 5a also shows that the retardance of the phase shifter made of achromatic waveplates is linearly related to the azimuth of the middle waveplate ($\lambda/2$). This relation has been theoretically derived in Evans (1949) (see equation VI.10 in that paper). The dashed curve shows the case of a phase shifter consisting of single-layer waveplates designed at 1523.1 nm, which is not linear at all. Although, it can be shown that a linear relation exists, if the wavelength of the incident light is exactly 1523.1 nm.

In some applications, the phase shifting rate is a matter of concern. The Newport RGV100 Series Motorized Rotation Stage has a rotation speed of 720° s^{-1} . This rotation speed results in a phase shifting

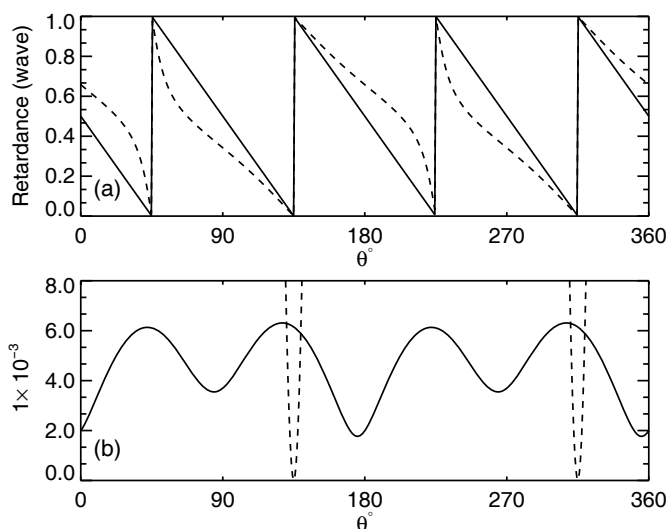


Fig. 5 Evens' three-waveplate phase shifter (Evans 1949) (see Sect. 4.1) using achromatic waveplates (solid curves). (a) Retardance vs. θ (azimuth of the half waveplate in the middle) and (b) the magnitudes of the off-diagonal elements of the Jones matrices of the two phase shifters. The dashed curves refer to the corresponding phase shifter composed of a set of three waveplates made from single-layer uniaxial crystals, designed to be $\lambda/4$ or $\lambda/2$ waveplates at 1523.1 nm. The solid curves correspond to a phase shifter made of three six-layer achromatic waveplates. The wavelength of the incident light is $\lambda = 1083.3$ nm.

rate of 8 waves s^{-1} , i.e., 125 ms $wave^{-1}$. Phase shifters can also be made from liquid crystal, i.e., then they are known as Liquid Crystal Variable Retarders (LCVR). For the Meadowlark LCVR, the response time to a half wave voltage is, according to the commercial documentations, 10 ms, which is much faster than mechanical rotation. The drawback of LCVRs is that the LC molecules on the surface switch faster than the molecules in the center of the LC cell by amounts depending on the thickness of the specific LC cell (usually a thin LC cell is sandwiched by two pieces of glass), and the phase change is not linearly controllable. The advantage of using an achromatic waveplate-based phase shifter other than an LCVR is it being a linear phase shifter, and more stable to hazardous environment, e.g., UV radiation (Ye 2004).

4.2 Waveplates for IRIM

Another example that applies broadband achromatic waveplates is the Near Infrared Imaging Magnetograph (IRIM) at Big Bear Solar Observatory (Denker et al. 2003a,b). The IRIM system utilizes a Fabry-Pérot interferometer, two birefringent filters, and a set of wide band interference filters. The two birefringent filters are designed for He I 1083 nm and Fe I 1565 nm respectively due to the chromatism of such optical components as waveplates, polarizers and coating. The optical components of the 1083 nm birefringent filter were designed to be removable, and therefore normal waveplates can be easily replaced by achromatic waveplates. The achromatic design of IRIM is challenging because the two lines are far apart. To solve this problem for the IRIM, we need to redefine the merit function as

$$E(\phi_k, \theta_k) = \sum_{\Delta\lambda_1} \sum_{ij} w_{ij} \Delta J_{ij} \cdot \Delta J_{ij}^* + \sum_{\Delta\lambda_2} \sum_{ij} w_{ij} \Delta J_{ij} \cdot \Delta J_{ij}^*, \quad (9)$$

where, $\Delta\lambda_1 = 1083 \pm 2$ nm and $\Delta\lambda_2 = 1560 \pm 2$ nm define the two achromatic regions, and $k = 3, 6, 10$ or any other desirable number of layers. $\mathbf{J} = J_k$ is the Jones matrix of the k -layer waveplate. As we have seen in previous sections, three-layer achromatic waveplates usually possess two local minima. This property can be tested here. Moreover, using the same crystal material, three is the minimum number of layers that is required to form a waveplate, and it will be a timesaving job to polish only three slices of crystal material.

We ran the simulated annealing program for this newly defined merit function, and found the following solution (in radians):

$$\begin{aligned}\theta_1 &= 0.53429, & \delta_1 &= 1.69690, \\ \theta_2 &= 2.45617, & \delta_2 &= 2.63967, \\ \theta_3 &= 0.53423, & \delta_3 &= 1.69677.\end{aligned}$$

We have carried out a numerical simulation for the third stage of the Lyot filter used in the IRIM with the same design parameters of the filter calculated by Wang et al. (2001). In this simulation, we tried the substitution of normal single-layer waveplates (half and quarter) by both the three-layer waveplates designed above and the six-layer waveplates in Table 1. The transmission profiles were calculated specifically in the vicinities of 1083 nm and 1565 nm, and the rotating half-waveplate is adopted as the bandpass tuning mechanism. We take two snapshots when the azimuth of the rotating waveplate are 0 and $\frac{2}{7}\pi$. The corresponding transmission profiles of a single stage Lyot filter are presented in Figure 6.

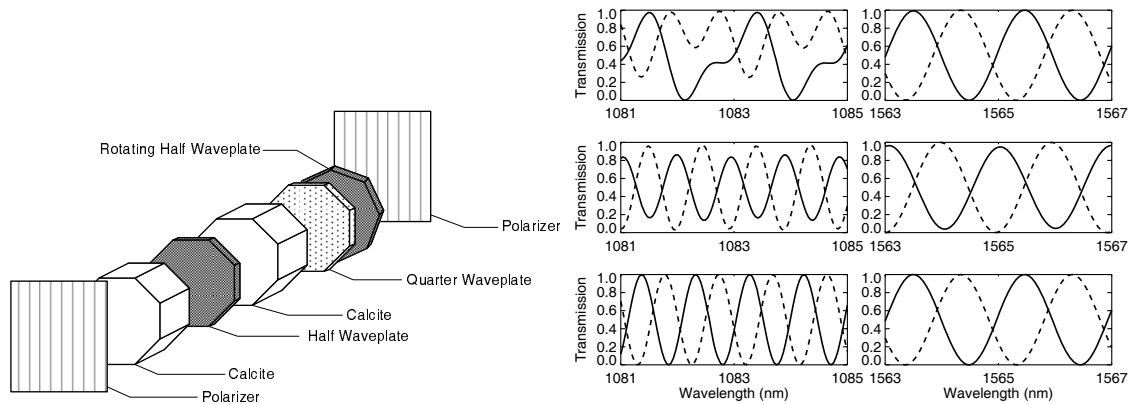


Fig. 6 Tuning of a single stage of a Lyot filter - single stage. Solid curves when the azimuth of the rotating $\lambda/2$ waveplate is set at 0; dotted curves, when set to $\frac{2}{7}\pi$. A cartoon of the single stage is shown on the left. On the right, the top row: transmission of the Lyot stage using single crystal waveplates; the middle row: using three-layer achromatic waveplates; the bottom: using six-layer achromatic waveplates.

There are two improvements to the bandpass profile of a birefringent filter by using n -layer achromatic waveplate — the bandpass symmetry and the off-band scattered light level (Fig. 6). To summarize,

- When single-crystal waveplates are used, the bandpass profile are symmetric only at the wavelength the waveplates are designed for, in this case, 1083 nm. Far away from this wavelength the bandpass profile turns to be asymmetric, while still possessing certain periodicity. In the middle panel on the right in Figure 6, the bandpass is shown with one period.
- The symmetry was improved on the bottom row in the case of using three-layer achromatic waveplates. However, it is obvious the scattered light level at both wavelength ranges are higher than in the single-crystal case. This proves that the three-layer waveplates are no longer functioning as waveplates. Although it was demonstrated in Figure 2 that the retardance of such three-layer waveplates could be perfect around two wavelengths, their roles of functioning as waveplates are broken if the azimuth of optical axes are taken into consideration. In other words, the three-layer waveplates designed in Table 1 or listed above are valid only when their optical axes are set at certain azimuth angles. This has nothing to do with the wavelength. Even when the setup is fixed at one single wavelength, such as in 1564 nm, three-layer waveplates, the waveplates are still very sensitive to the azimuth of their own optical axes.
- In the case of using six-layer achromatic waveplates, both the symmetry and the scattering light are improved. The bandpass profiles are close to the case of using the ideal achromatic waveplates.

From this simulation, we can draw our conclusions regarding the application of n -layer achromatic waveplates in Lyot filter. The three-layer waveplates can not be used in Lyot filter due to very high off-band scattered light level. The off-band light is out of the control of the filter design, and therefore will impair the performance of Lyot filter and the IRIM system in an unpredictable way. The six-layer achromatic waveplates can be an ideal choice for application in Lyot filters. We did not considering number of layers less than six, but the simulated annealing procedure is general enough that it can handle any number of layers in the design of n -layer achromatic waveplates.

After the substitution of the waveplates in Lyot filter with six-layer achromatic waveplates and the elimination of the chromatism in the other optical components, the working range of the 1083 nm-Lyot filter at BBSO can be expanded to the whole wavelength range from 1000 nm to 1800 nm. Using the solutions of multilayer waveplates provided in the present paper, the filter design can be greatly simplified.

5 EXPERIMENT ON WAVEPLATES

The scheme shown in Figure 3 is one of the methods that can be used in measuring the retardance of a waveplate, assuming its optical axis is known beforehand. Since the light after passing through the polarizer and a $\lambda/4$ is elliptically polarizer due to imperfections in the waveplate, the output intensity varies with the azimuth of the analyzer periodically. The maximum and minimum of the intensity can be selected, they are proportional to a^2 and b^2 shown in Figure 3. The ratio a/b is the ellipticity. Note that another commonly used measure of the elliptical shape is the eccentricity ϵ , defined by $\epsilon = \sqrt{1 - b^2/a^2}$. The retardance δ of the waveplate can be derived from the ellipticity and the incline angle ψ .

The following relations between the angles in Figure 3 can be easily obtained (see, for example, Born & Wolf 1999):

$$\sin 2\chi = \sin 2\alpha \sin \delta, \quad (10)$$

$$\tan 2\psi = \tan 2\alpha \cos \delta, \quad (11)$$

from which we can derive

$$\sin 2\alpha = \sqrt{(\sin^2 2\chi + \tan^2 2\psi) / (1 + \tan^2 2\psi)}, \quad (12)$$

where $0 \leq \alpha \leq \pi/2$ by definition. In this relation, ψ is the azimuth of the analyzer where the output intensity is maximum and can be measured experimentally. Also,

$$\tan \chi = \mp b/a, \quad (13)$$

which is related directly to the measurable ellipticity. Therefore, the angle α can be found, and hence the retardance δ . Moreover, the following complications should be noted:

$$0 < \psi < \pi/2, \text{ if } 0 < \delta < \pi/2; \quad (14)$$

$$\pi/2 < \psi < \pi, \text{ if } \pi/2 < \delta < \pi. \quad (15)$$

When using Equation (10) to derive δ , we take

$$\delta = \sin^{-1} \left(\frac{\sin 2\chi}{\sin 2\alpha} \right), \text{ if } 0 < \psi < \pi/2, \quad (16)$$

$$\delta = \pi - \sin^{-1} \left(\frac{\sin 2\chi}{\sin 2\alpha} \right), \text{ if } \pi/2 < \psi < \pi. \quad (17)$$

These two relations were implemented in deriving Figure 2.

Table 2 Achromatic Three-Layer Waveplates

Half AWP	Azimuth	Thickness (mm)
1 (thick)	60° 9'59"	0.5755 (0.595)
1 (thin)	150° 9'59"	0.5000 (0.519)
2 (thick)	118°20'53"	0.5755 (0.595)
2 (thin)	28°20'53"	0.5000 (0.519)
3 (thick)	60° 9'59"	0.5755 (0.595)
3 (thin)	150° 9'59"	0.5000 (0.519)
Quarter AWP		
1 (thick)	62°55' 4"	0.5617 (0.561)
1 (thin)	152°55' 4"	0.5000 (0.499)
2 (thick)	135°25'22"	0.5924 (0.610)
2 (thin)	45°25'22"	0.5000 (0.519)
3 (thick)	62°55' 4"	0.5617 (0.561)
3 (thin)	152°55' 4"	0.5000 (0.499)

6 TESTING RESULTS

A set of multi-layer waveplates were manufactured by the Nanjing Institute of Astronomical Instrumentation of China, according to the parameters shown in Table 2. The parameters of the achromatic waveplates here belong to an earlier version of design, in which some details, such as the reference wavelength, are missing. However, the experimental data have been used for the present paper.

Two calibrated near infrared linear polarizers are used in two combinations: crossed and parallel. The sample of waveplates is inserted in between with an angle 45° to the active axis of the first polarizer. Note that a half waveplate can rotate linear polarized light by 90° if the relative angle between the light and the optical axis of the waveplate is 45°. Suppose we have inserted a perfect half waveplate, then the output intensity should be maximum if the polarizers are crossed, and minimum if the polarizers are parallel. The three-layer quarter waveplate was not tested as a quarter waveplate. Instead, two such quarter waveplates were combined together and tested as a half waveplate. Therefore, this test can only prove that the three-layer waveplate is a half waveplate or quarter waveplate, but the retardance is not measured.

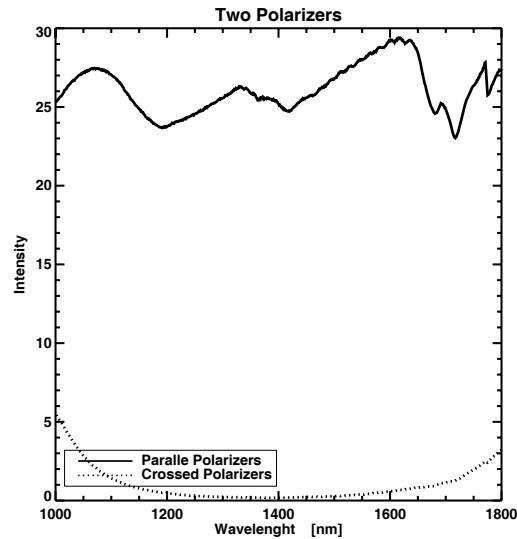


Fig. 7 Properties of near infrared linear polarizers in crossed and parallel configurations. Also, the profile of the light source involved in these profiles.

The testing results of a set of three-layer waveplates are plotted in Figures 7, 8 and 9. The wavelength dependence of the waveplate in Figure 9 was shown to be reduced compared to traditional single layer waveplates. The test proves that the three-layer waveplates do approach the achromatic waveplate. Increasing the number of layers is a promising direction to achieve achromatism in waveplates.

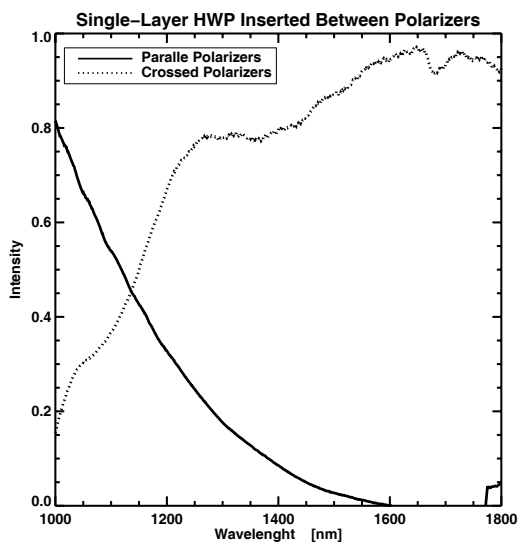


Fig. 8 Testing results for a normal single-layer half waveplate using the polarizers and light source shown in Fig. 7.

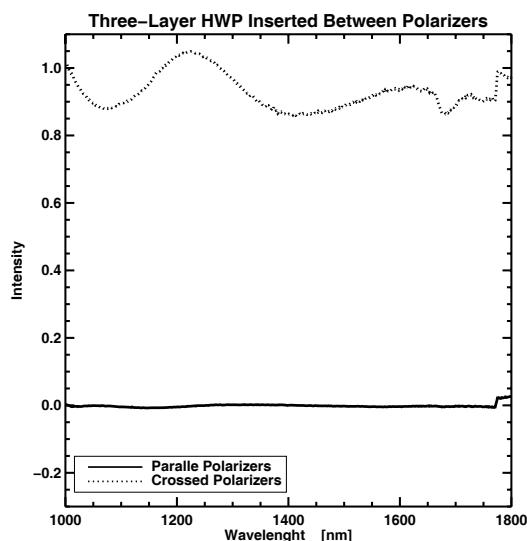


Fig. 9 Testing result of the three-layer half waveplate with the parameters listed in Table 2.

7 CONCLUSIONS

We presented a procedure based on Monte Carlo simulated, annealing algorithm to design crystalline multilayer achromatic waveplates. We applied the procedure to three examples of multilayer waveplate, three-, six- and ten-layer waveplates, and obtained the parameters listed in Table 1. Either the six- or ten-layer structures can produce high quality $\lambda/4$ and $\lambda/2$ achromatic waveplates over wide wavelength regions. Specifically, the issue of optical-axis in the three-layer waveplate is minimized in the six- and ten-layer waveplates (see Fig. 2). The performance of such n -layer achromatic waveplates was numerically evaluated in terms of the residual errors in the Jones/Mueller matrix elements and the polarization errors in the Stokes vectors. Using these six- or ten-layer achromatic waveplates, an achromatic phase shifter can be constructed based on a simple structure proposed by Evans (1949). This phase shifter produces continuous fractional phase change from 0 to 2π within the spectral range considered, thus providing a reliable solution for many tuning instruments, particularly in our case of the tunable birefringent filters.

It might turn out that thin material wafers with stress birefringence (photo-elastic effect (Born & Wolf 1999)) is an alternative to quartz or calcite. Wafers of stress birefringent materials are traditionally polymers, such as poly-methyl-methacrylate (PMMA), polyvinyl chloride (PVC) or polycarbonate (PC) (Delplancke et al. 1995). These polymer materials have different transmission properties in different spectral ranges. Therefore, the transmission might not be as high as uniaxial crystals. Moreover, care should be taken using these non-crystalline materials. The reason is that the parameters shown in Table 1 are designed based on the assumption that the “retardance vs. wavelength” relation is as shown in Equation (2), which would need to be re-evaluated for non-crystalline materials. In this case, we have to know the exact $\delta - \lambda$ function. However, the SA algorithm is sufficiently flexible to allow the implementation of different $\delta - \lambda$ functions.

Acknowledgements JM wants to thank Dr. D. G. Wang in the Huairou Solar Observatory, NAOC, for helpful discussions on the choices of the material for making the multilayer waveplates. We are also grateful to the staff members of Nanjing Institute of Astronomical Instrumentation (China) for manufacturing the three-layer waveplates. This work was supported by NSF under grants ATM 03-42560, ATM 02-36945, IIS ITR 03-24816, AST MRI 00-79482, and by NASA under grant NNG0-6GC81G.

References

- Beckers J. M., 1971, *Appl. Opt.*, 10, 973
 Beckers J. M., 1972, *Appl. Opt.*, 11, 681
 Beckers J. M., Dickson L., Joyce R. S., 1975, *Appl. Opt.*, 14, 2061
 Born M., Wolf E., 1999, *Principles of optics : electromagnetic theory of propagation, interference and diffraction of light / Max Born and Emil Wolf; with contributions by A. B. Bhatia et al.* Cambridge [England]; New York: Cambridge University Press, 1999
 Cao W., Hartkorn K., Ma J. et al., 2006, *Sol. Phys.*, 238, 207
 Delplancke F., Bernaerd R., Ebbeni J., Sendrowicz H., 1995, *Appl. Opt.*, 34, 2921
 Denker C., Didkovsky L., Ma J. et al., 2003, *Astronomische Nachrichten*, 324, 332
 Denker C. J., Ma J., Wang J. et al., 2003, *Proc. SPIE*, 4853, 223
 Denker C. et al., 2006, *Proc. SPIE*, 6267
 Evans J. W., 1949, *Journal of the Optical Society of America (1917-1983)*, 39, 229
 Filinski I., Skettrup T., 1984, *Appl. Opt.*, 23, 2747
 Flanders D. C., 1983, *Applied Physics Letters*, 42, 492
 Ghosh G., 1999, *Optics Communications*, 163, 95
 Guimond T., Elmore D., 2004, *SPIE's OE Magazine*, 4, 26
 Goode P. R., NST Team, 2006, *AAS/Solar Physics Division Meeting*, 37, 37.01
 Habib A., Vernin J., Benkhaldoun Z., Lanteri H., 2006, *MNRAS*, 367
 Hariharan P., 1995, *Measurement Science and Technology*, 6, 1078
 Ingber L., 1996, *Control and Cybernetics*, 33, 25
 Keil S. L., Rimmele T. R., Keller C. U., the Atst Team, 2001, *ASP Conf. Ser. 236: Advanced Solar Polarimetry – Theory, Observation, and Instrumentation*, 236, 597
 Keil S. L., Rimmele T. R., Oschmann J., the Atst Team, 2005, *IAU Symposium*, 223, 581
 Kikuta H., Ohira Y., Iwata K., 1997, *Appl. Opt.*, 36, 1566
 Kirkpatrick S., Gelatt C. D., Vecchi M. P., 1983, *Science*, 220, 671
 Kuhn J. R., Balasubramaniam K. S., Kopp G. et al., 1994, *Sol. Phys.*, 153, 143
 Ma J., Wang J., Cao W. et al., 2004, *Proc. SPIE*, 5523, 139
 McIntyre C. M., Harris S. E., 1968, *Journal of the Optical Society of America (1917-1983)*, 58, 1575
 Munakata T., Nakamura Y., 2001, *Phys. Rev. E*, 64, 046127
 Newman M. E. J., Barkema G. T., 1999, *Monte Carlo methods in statistical physics*, Oxford: Clarendon Press, 1999
 Pancharatnam S., 1955, *Proc. Indian Acad. Sci.*, A41, 137
 Rimmele T. R. et al., 2005, *Proc. SPIE*, 5901, 41
 Shurcliff W. A., 1966, Cambridge, Mass: Harvard University Press, —c1966
 Spirock T. J., 2005, Ph.D. Thesis, Big Bear Solar Observatory & New Jersey Institute of Technology
 Sun P., Yin Y., Li B. et al., 2005, *Phys. Rev. E*, 72, 061408
 Title A. M., 1975, *Appl. Opt.*, 14, 229
 Wang J., Wang H., Goode P. R. et al., 2001, *Optical Engineering*, 40, 1016
 Ye C., 2004, *Appl. Opt.*, 43, 4007